MODELLING AND ASSESSMENT OF THE IMPACT OF NEW SPACE SURVEILLANCE SYSTEMS ON SUSTAINABLE SPACECRAFT OPERATIONS

Aleksandar Kovacic[(1)], Jan Siminski[(2)], Klaus Merz[(2)], Simon Burgis[(3)], Reinhold Bertrand[(4)]

[(1)] Institute of Flight Systems and Automatic Control, Technical University of Darmstadt, Otto-Berndt-Straße 2, Darmstadt, 64287, Germany, Email: aleksandar.kovacic@outlook.de
[(2)] Space Debris Office, ESA/ESOC, Robert-Bosch-Str. 5, Darmstadt, Germany, Email: {jan.siminski, klaus.merz}@esa.int
[(3)] Institute of Flight Systems and Automatic Control, Technical University of Darmstadt, Otto-Berndt-Straße 2, Darmstadt, 64287, Germany, Email: burgis@fsr.tu-darmstadt.de
[(4)] Joint Professorship Space Systems between Institute of Flight Systems and Automatic Control and European Space Agency ESA/ESOC, TU Darmstadt, Otto-Berndt-Straße 2, Darmstadt, 64287, Germany, Email: reinhold.bertrand@esa.int

ABSTRACT

With the increased performance of the US space surveillance network (SSN) through the Space Fence, the number of detectable objects is expected to increase. The manoeuvre rate a mission operator has to perform in order to avoid collisions depends on the number of detectable space objects. The aim of this work is to use ESA's Assessment of Risk Event Statistics (ARES) software to compute the expected manoeuvre rate resulting from the improved performance of the SSN.

In the second part of this work, uncertainty requirements of future space surveillance systems were derived to ensure sustainable spacecraft operations. For this purpose, a simplified sustainability score was developed that assesses the impact of a collision on the space environment, in terms of the likelihood and the consequence of a collision. The most demanding uncertainty requirement derived is 12.25 m in along-track direction at an altitude between 550 and 800 km.

1 INTRODUCTION

In order to avoid collisions with space debris, the position of these objects has to be determined by means of several sensor systems such as radar, telescope and laser systems. The United States (US) Space Surveillance Network (SSN) is the largest sensor network to detect, track, catalogue and identify space debris, which is depicted in Figure 1.1 [1].

Figure 1.1 The US Space Surveillance Network (SSN) [2]

It maintains the most complete catalogue of space objects and is operated by the US Space Force [3]. With the introduction of the new Space Fence phased array radar system (red square in Figure 1.1), the SSN receives an extension of its sensor network in order to increase the space object detection sensitivity, coverage and tracking accuracy. The Space Fence will consist of two sensor sites located on Kwajalein Atoll and in Western Australia, which is depicted in Figure 1.2.

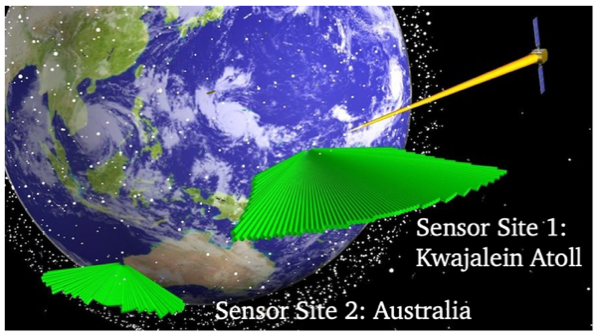

Figure 1.2 Space Fence system sensor site [4]

The sensor site on Kwajalein Atoll achieved operational capability and acceptance on 27 March 2020. It is a ground-based S-band phased array radar, which is capable of providing coverage in LEO with its un-cued surveillance fence [4]. The Space Fence will also provide cued tasking support to detect and track objects of all altitudes including GEO [4]. The introduction of the Space Fence results in the detection of more objects than before, which leads to an increase in manoeuvre rate of satellites. This increase of the manoeuvre rate is operationally challenging and needs to be addressed in the framework of this work.

In the second part of this work a sustainability score was developed that assesses the impact of a collision on the space environment by combining the consequence of a collision with the likelihood that this collision will occur. The consequence is defined as the number of fragments created during the collision. The likelihood is provided by ESA's Assessment of Risk Event Statistics (ARES)

software in form of several annual collision probability metrics, which will be demonstrated later in this work. The consequence and likelihood values are then classified into a likelihood and consequence score, with the product of both, forming the sustainability score or simply called "risk". Based on the results provided by the sustainability rating it is possible to derive requirements of future space surveillance networks. Especially when using the residual risk for the likelihood, it is possible to derive uncertainty requirements.

2 SPACE FENCE PERFORMANCE MODELLING IN ARES

With the initial operational capability and operational acceptance of the Space Fence on March 27th 2020, the catalogue size of the SSN is expected to increase by a factor of 2 [5, 6]. One of the objectives of this work is to determine the increase in the number of avoidance manoeuvres ESA has to perform based on the additional measurements provided by the new Space Fence. Such a simulation can be conducted by means of ESA's ARES software. ARES requires several input parameters in order to describe the performance of the SSN upgraded with the new Space Fence. This includes the reference diameter D_{ref}, the radar wavelength λ and the covariance matrix $\boldsymbol{C}$. However, these parameters are subject to uncertainty, which makes the prediction of the final performance challenging. Even if the performance parameters are not exactly known, for some of these parameters approximate values can be found in literature, which will be presented in the following section.

Reference diameter D_{ref}

There are different specifications regarding the reference diameter D_{ref} provided by current literature. The reference diameter describes the smallest detectable diameter of space objects given at a certain reference altitude h_{ref}. Table 2.1 gives an overview of the various D_{ref} values depending on the altitude found in literature. The term un-cued refers to the process of detecting objects in space with no a-priori knowledge of their orbit [7].

Table 2.1 Expected reference diameter D_{ref} of the new Space Fence based on literature

D_{ref}	h_{ref}	Source
2 cm – 9 cm	400 km	[8]
2 cm – 5 cm	-	[9]
5 cm	0 – 2000 km	[5]
1 cm (cued), 9.7 cm (un-cued)	-	[10]
1 cm	0 – 2000 km (LEO)	[11]

Wavelength λ

The new Space Fence will be the first S-band surveillance radar operated entirely for the purpose of detecting and tracking objects in space [12]. This means that the wavelength model parameter is in a range between 0.075 m and 0.15 m [13].

The blue line in Figure 2.1 represents the performance of the current SSN with a wavelength of 0.3 m and a reference diameter D_{ref} of 0.32 m at a reference altitude h_{ref} of 2000 km.

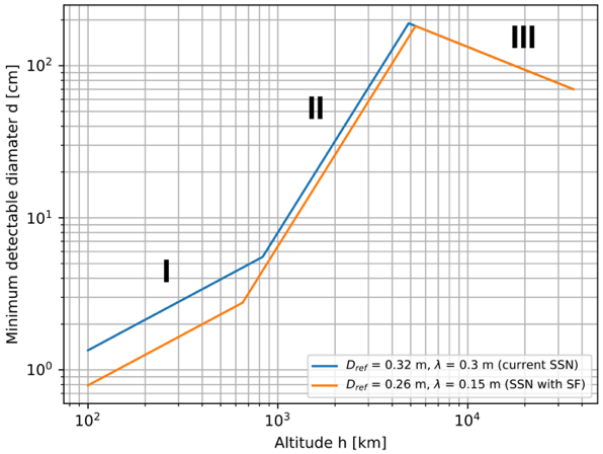

Figure 2.1 SSN performance for the current SSN in blue and the SSN with the new Space Fence in orange, both at a reference altitude h_{ref} of 2000 km.

The SSN performance curve in Figure 2.1 is determined by following set of equations

$$D_{min}^{*} = \max(D_{min}, D_R), \tag{1}$$

where D_R is the equation for small body approximations

$$D_R = \sqrt[6]{\sigma \cdot \frac{4}{9} \cdot \frac{\lambda^4}{\pi^5}}, \tag{2}$$

with the radar cross section (RCS) σ

$$\sigma = \frac{1}{4} \cdot \pi \cdot D_{ref}^2 \cdot \left(\frac{h}{h_{ref}}\right)^4 \tag{3}$$

and

$$D_{min} = \min\left(D_{min,r}, D_{min,o}\right), \tag{4}$$

where

$$D_{min,r}(h) = D_{ref} \cdot \left(\frac{h}{h_{ref}}\right)^2 \tag{5}$$

describes the radar performance and

$$D_{min,o}(h) = D_{ref,o} \cdot \left(\frac{h}{h_{ref,o}}\right)^{0.5} \quad (6)$$

describes the performance of passive optical systems. For further details regarding the mentioned equations, see [14].

Since this paper analyses the impact of the new Space Fence, which is a radar system, equation (6) will be neglected.

In order to derive a reference radar equation representing the performance of the new Space Fence, the wavelength and the reference diameter will be selected in a way that it will satisfy the 2 cm expectation of [8] at a reference altitude of 400 km (see Table 2.1). This requirement is also compliant with most of the other specifications given in Table 2.1 and it is achievable by setting the wavelength to a value of 0.15 m and the reference diameter to 0.26 m at a reference altitude of 2000 km. The reference equation for the new SSN is depicted as orange line in Figure 2.1.

Covariance C

The covariance in ARES is divided into several orbital classes. There are three size classes, which are determined by the radar cross section (RCS), two eccentricity classes, six altitude classes and six inclination classes. The class definitions are listed in Table 2.2 and Table 2.3.

Table 2.2 Uncertainty class definitions in ARES for size and eccentricity [14]

Size (RCS) [m^2]	Eccentricity
$s_1 < 0.1$	$e < 0.1$
$0.1 \leq s_2 < 1.0$	$e \geq 0.1$
$s_3 > 1.0$	

Table 2.3 Uncertainty class definitions in ARES for perigee altitude and inclination [14]

Perigee altitude [km]	Inclination [°]
$h_{p1} \leq 350$	$0 < i \leq 15$
$350 < h_{p2} \leq 550$	$15 < i \leq 30$
$550 < h_{p3} \leq 800$	$30 < i \leq 45$
$800 < h_{p4} \leq 2000$	$45 < i \leq 60$
$2000 < h_{p5} \leq 25000$	$60 < i \leq 75$
$h_{p6} > 25000$	$75 < i \leq 90$

Every orbital class contains three uncertainty values, which include the along-track (AT), cross-track (CT) and radial (RA) component as seen in Table 2.4. In ARES it is possible to pass covariance data in form of Table 2.4 by providing own covariance data or by using internal ARES values, which have been derived from conjunction data messages (CDM). It has to be mentioned, that, for reasons of clarity, the two size classes (s_2 and s_3) have been omitted from Table 2.4.

Table 2.4 Uncertainty class definition in ARES [14]

Small objects s_1		i_1	i_2	i_3	i_4	i_5	i_6
e < 0.1	h_{p1}	AT CT RA	AT CT RA	AT CT RA	AT CT RA	AT CT RA	AT CT RA
	h_{p2}	…	…	…	…	…	…
	h_{p3}	…	…	…	…	…	…
	h_{p4}	…	…	…	…	…	…
	h_{p5}	…	…	…	…	…	…
	h_{p6}	…	…	…	…	…	…
e > 0.1	h_{p1}	…	…	…	…	…	…
	h_{p2}	…	…	…	…	…	…
	h_{p3}	…	…	…	…	…	…
	h_{p4}	…	…	…	…	…	…
	h_{p5}	…	…	…	…	…	…
	h_{p6}	…	…	…	…	…	…

Furthermore, it is possible to define a scaling factor table which makes it possible to manipulate the values in the covariance table by multiplying them with a scaling factor. This scaling factor table is of the same form as the covariance table but applies one scaling factor to all three values (AT, CT and RA). The scaling factor table is depicted in Table 2.5 with an exemplary factor of 1.0 for every cell (which means no scaling at all).

Table 2.5 Scaling factor table

Small objects s_1		i_1	i_2	i_3	i_4	i_5	i_6
e < 0.1	h_{p1}	1.0	1.0	1.0	1.0	1.0	1.0
	h_{p2}	…	…	…	…	…	…
	h_{p3}	…	…	…	…	…	…
	h_{p4}	…	…	…	…	…	…
	h_{p5}	…	…	…	…	…	…
	h_{p6}	…	…	…	…	…	…
e > 0.1	h_{p1}	…	…	…	…	…	…
	h_{p2}	…	…	…	…	…	…
	h_{p3}	…	…	…	…	…	…
	h_{p4}	…	…	…	…	…	…
	h_{p5}	…	…	…	…	…	…
	h_{p6}	…	…	…	…	…	…

In order to determine which uncertainty classes will improve through the implementation of the new Space Fence, a simulation conducted by Lockheed Martin, which is described in [12] was analyzed. The analysis shows that the new Space Fence has the capability to detect objects in the following orbital regions, which were used to determine the orbital uncertainty classes, which need to be adjusted in Table 2.4 or Table 2.5. This includes following classes:

- Perigee altitude < 3000 km
- Eccentricity < 0.1
- 0° < Inclination < 110°

These classes are marked yellow in Table 2.5.

From [5] it is known that the catalogue size will probably be doubled and that the covariance will change due to three reasons:

1. Well-tracked objects will receive additional tracking. This will reduce the uncertainty only slightly since these objects are already well maintained [5]
2. Poorly tracked objects (by the current SSN) will have their tracking doubled, which results in smaller covariances [5].
3. New objects will be trackable only by the new Space Fence, which results in large covariances for these objects [5].

Since the covariance is expected to both decrease and increase (see bullet points 2 and 3), a reference value of 1 is assumed as default scaling factor. This means that the default case of the Space Fence does not consider any improvement or deterioration of the uncertainty. It is initially set to 1 but will be varied in separate analysis. Table 2.6 gives an overview of the reference parameters describing the SSN performance increase due to the new Space Fence. In addition to that, Table 2.6 also includes the parameters of the old SSN without the Space Fence for the purpose of comparability.

The calculation and the meaning of these output parameters are explained in detail in [14].

Table 2.6 Reference parameters for the Space Fence

SSN	D_{ref}	h_{ref}	Wavelength	Scaling Factor
New SSN	0.26 m	2000 km	0.15 m	1
Old SSN	0.32 m	2000 km	0.3 m	1

Orbital / Spacecraft parameters

Due to the fact that most of the space debris in the space environment currently resides in altitude regions between 700-900 km, a satellite orbiting at this altitude will be analyzed in the first instance [15]. For the first analysis, the orbital parameters of ESA's Earth observation satellite Sentinel-3A were chosen to serve as reference parameters. However, the selection is of less importance, since the parameters are varied anyway. Table 2.7 gives an overview of these reference parameters.

Table 2.7 Orbital reference parameters for Sentinel-3A [16]

Parameter	Value
Spacecraft radius r	NDA (non-disclosure agreement)
Altitude h	803 km $\left(\text{defined as } h = \frac{h_a + h_\pi}{2}\right)$
Right ascension of ascending node Ω	280.2164°
Argument of perigee ω	97.7552°
Inclination i	98.6204°
Eccentricity e	0.00011490

Based on these input parameters (D_{ref}, λ, $\boldsymbol{C}$ and orbital parameters) and other input parameters from [17], ARES provides several output parameters that are important for the assessment of the performance of space surveillance systems. The most important output parameters, that have been used in this work, are:

Table 2.8 Output parameters provided by ARES

Output parameter	Formula symbol
Annual manoeuvre rate	M_A
Annual collision probability due to the whole population	ACP_w
Annual collision probability due to detectable objects	ACP_d
Annual Collision Probability due to detectable objects, which involve collisions with an energy to mass ratio (EMR) larger than a specific threshold	ACP_{EMR}
Residual Risk	R
Risk Reduction	Q
Remaining Risk	S
Fractional Residual Risk	FRR
Fractional Risk Reduction	FQR
Fractional Remaining Risk	FSR

3 PYTHON SCRIPT FOR PARAMETRIC VARIATIONS

ARES uses a graphical user interface (GUI) with which it is possible to pass the input parameters and receive the output parameters. However, this method has the disadvantage that only one value can be defined for each parameter. For example, it is not possible to pass multiple inclination values with the GUI to ARES in order to perform parametric variations. However, this is possible with the Python library pyDRAMA, which enables parametric variations to be performed in ARES. This allows, for example, a list of inclination values or any other parameter to be passed to ARES in order to calculate a result for each possible combination. However, this method is also limited because it is not possible to adjust the wavelength λ, the reference diameter D_{ref}, the accepted collision probability level (ACPL) and the covariance data and to pass a list of values for these parameters. Therefore, a Python script was developed which uses the ARES module from the pyDRAMA library but is extended by functions which make it possible to change the mentioned parameters and to pass a list of values for parametric variations. The developed functions access the ARES input text file (ares.inp) and change the values in it. After the values have been transferred to ARES and ARES has computed the output parameters, the output data is collected and saved in a clear csv file. Figure 3.1 shows a flow chart of the Python/ARES interface structure on a basic level. Furthermore, it shows that ARES obtains information about the space debris environment through ESA's Meteoroid and Space Debris Terrestrial Environment Reference model (MASTER). The same figure also indicates that the ARES output was also used in the development of the sustainability score, which will be subject later in this work.

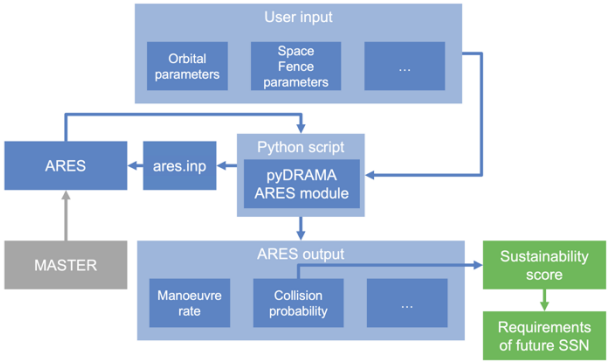

Figure 3.1 Python/ARES interface flow chart

4 RESULTS OF SPACE FENCE PERFORMANCE MODELLING IN ARES

Figure 4.1 shows the manoeuvre rate of the old SSN (i.e. SSN without Space Fence) for the epoch 01-11-2022 depending on the inclination and the altitude.

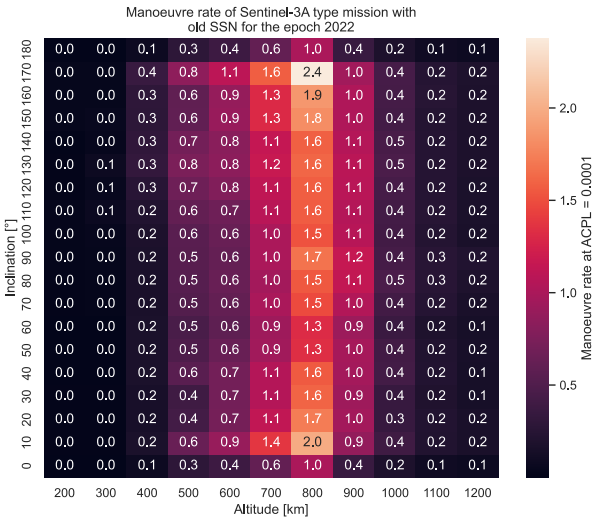

Figure 4.1 Manoeuvre rate for an ACPL of 0.0001 for the old SSN in 2022 depending on the inclination and the altitude.

The manoeuvre rate is displayed for an ACPL of 0.0001. The selection of this ACPL is a result of achieving a certain risk reduction. The general approach of ESA is to define the ACPL for LEO missions based on a **relative risk reduction** (relative, also called fractional) of 90% but it is also possible to define it in terms of absolute values such as the **risk reduction** [18, 19]. Common ACPL values in LEO range from 10^{-5} to 10^{-4} [15]. An alternative approach consists of using an a-priori threshold given by the mission owner [18]. All of these approaches lead to an ACPL, which determines the

manoeuvre rate as described in [14]. Throughout the following plots a constant ACPL of 0.0001 will be used, which is a common threshold that many operators use for missions in LEO [18]. This figure has become a quasi-standard for LEO missions but is also used for ESA's Sentinel constellation [18]. In reality different ACPLs are being used for different orbital altitudes. However, the use of a constant ACPL enables to analyse the manoeuvre rate of a Sentinel type mission if it would orbit in several different altitudes and inclinations with a constant ACPL. Furthermore, this provides a very clear presentation of the manoeuvre rate in the following heat maps.

It is visible, that the manoeuvre rate is highest at altitudes between 700 km and 900 km. This is due to the fact that the spatial density is highest at these orbital heights as Figure 4.2 shows. It depicts the spatial density distribution for objects larger than 1 cm for the population on 01-11-2022. The spatial density is highest for the three orbital altitudes at 700 km, 800 km and 900 km. To the left and right of these altitude hotspots, the manoeuvre rate decreases again because the spatial density decreases.

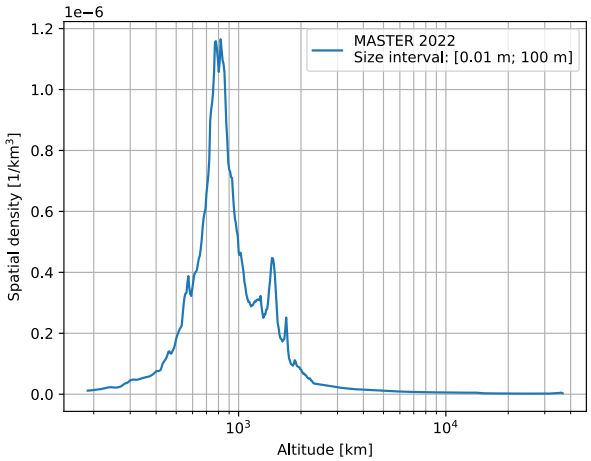

Figure 4.2 Spatial density contributions for objects larger than 1 cm for the epoch 2022.

According to this logic, the manoeuvre rate should decrease for orbital regions with high inclinations, since the spatial density decreases with increasing inclination as it is depicted in Figure 4.3 (Note, that the declination is given in a range between -90° and 90°, whereas the inclination is given in a range between 0° and 180°. Since both angles use the equatorial plane as reference plane, the declination can be used to estimate the spatial density in terms of the inclination).

The reason behind the increasing manoeuvre rate is that the uncertainty increases at very high and very low inclinations due to the sensors being distributed at higher latitudes, which results in a worse observability [20]. Furthermore, there is simply less data for these orbits as fewer missions reside at these inclinations.

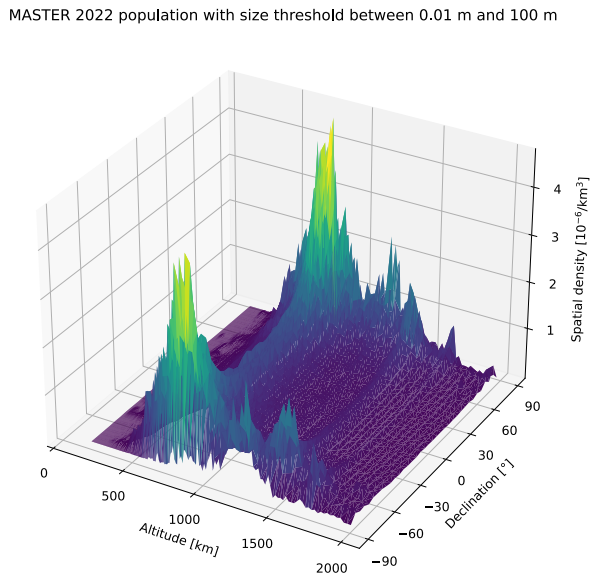

Figure 4.3 Spatial density for objects larger than 1 cm as a function of altitude and declination for the epoch 2022.

The next step consists of simulating the manoeuvre rates based on the input parameters for the new Space Fence as listed in Table 2.6. Figure 4.4 depicts that the new Space Fence increases the manoeuvre rate with the mentioned input parameters. This can be recognized from the colour bar on the right side, where the upper limit is greater than 3.0, whereas the upper limit in Figure 4.3 is greater than 2.0. The manoeuvre rate increases because more objects are detectable due to the reduction of the radar wavelength λ to 0.15 m and the reference diameter D_{ref} to 0.26 m.

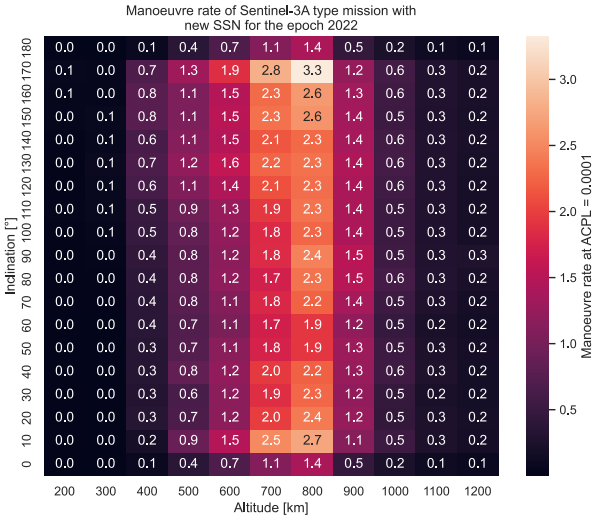

Figure 4.4 Manoeuvre rate for an ACPL of 0.0001 for the new SSN in 2022 depending on the inclination and the altitude

In order to evaluate the performance of the Space Fence in a future scenario Figure 4.5 provides the manoeuvre

rate for the population in 2036. This is the last year for which MASTER offers a population propagation. This means that MASTER has the possibility to propagate the population 14 years into the future counting from the current year 2022.

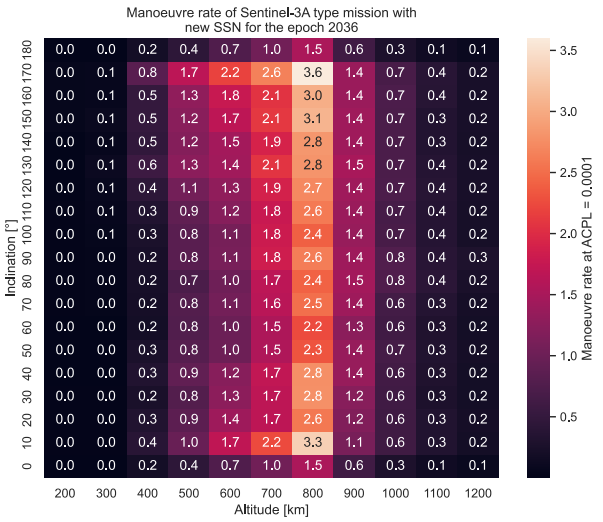

Figure 4.5 Manoeuvre rate for an ACPL of 0.0001 for the new SSN in 2036 depending on the inclination and the altitude

Figure 4.5 shows that the manoeuvre rate level increases to over 3.5, which is a small change compared to the manoeuvre rate level of approximately 3.0 for the epoch 2022 in Figure 4.4. This shows that the debris flux increase throughout the years is moderate for the altitude at 800 km and above. For the heights below 800 km, there is even a decline in the debris flux, i.e. the manoeuvre rate to observe. This is due to the fact that the spatial density distribution for 2036 is predicted by MASTER as depicted in Figure 4.6.

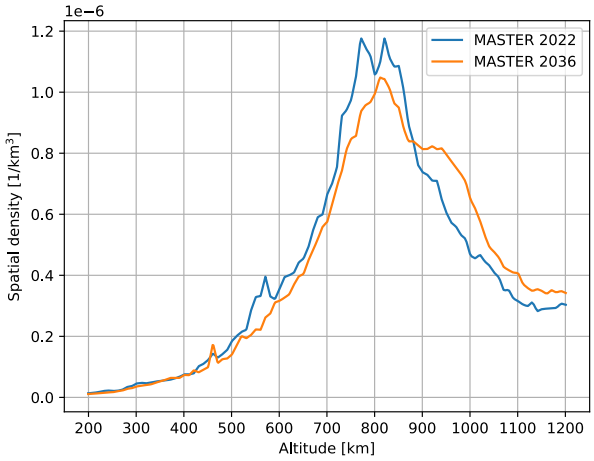

Figure 4.6 Spatial density distribution depending on the altitude for objects with a size between 0.01 m and 100 m.

Nevertheless, the manoeuvre rate will increase in the heavily polluted region of 800 km for the selected input parameters, which is alarming. Special attention must be paid to the fact that the uncertainty of the Space Fence is not predictable at the moment. As already mentioned, a scaling factor of 1 was used throughout these plots. Therefore, the next step consists of analysing the effect of uncertainty variations on the manoeuvre rate.

Figure 4.7 shows the manoeuvre rate for different scaling factors, i.e. different uncertainties and altitudes. Note that the inclination on the vertical axis has been replaced by the scaling factor and that the diagram was generated using a fixed inclination of 90°. The scaling factor limits were set to 0.5 and 2. The lower limit was set to 0.5 since poorly tracked objects (by the current SSN) will have their tracking doubled, whereas the upper limit was set to 2 since new objects will be trackable only by the new Space Fence, which results in large covariances for these objects [5].

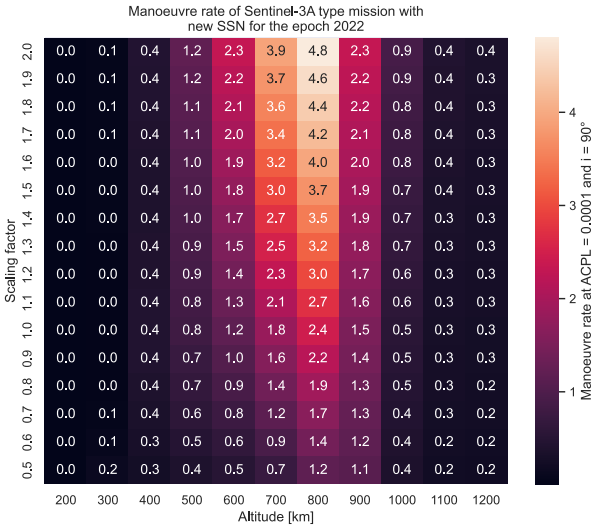

Figure 4.7 Manoeuvre rate for an ACPL of 0.0001 for the new SSN in 2022 depending on the scaling factor and the altitude

Figure 4.7 shows the influence of the scaling factor on the manoeuvre rate for the epoch 2022. When assuming that at an altitude of 800 km the scaling factor does change from 1 to 0.5 (i.e. an uncertainty improvement), the manoeuvre rate decreases from 2.4 to 1.2. If the uncertainty worsens, i.e. the factor increases from 1 to 2, the manoeuvre rate will increase.

For a scaling factor of 0.5 the number of manoeuvres is acceptable. It even decreases compared to the current SSN. However, if the covariance turns out to be higher, multiple manoeuvres will have to be performed by the operator.

Nevertheless, there is a more important insight than just the raw the numbers. From Figure 4.4 and Figure 4.7 it is

observable that an improvement of the smallest detectable diameter and the wavelength increase the manoeuvre rate, whereas an improvement of the uncertainty decreases the manoeuvre rate, which is why it deserves special treatment in terms of requirement derivation. Furthermore, it is assumed that the Space Fence will be the best radar system in the next few years, which is why the uncertainty requirements will be derived based on the Space Fence performance. The objective is to find out how far the uncertainty has to be improved in order to secure sustainable spacecraft operations with the modified SSN. In order to answer this question and to derive the uncertainty requirements a simplified sustainability score will be developed in the second part of this work.

5 SUSTAINABILITY SCORE DEVELOPMENT

As the number of objects in space increases, concerns arise that the space environment will be unsafe or even no longer usable in the future. The Kessler syndrome breakout is one of the biggest fears of the space community. Looking at the new satellite mega-constellations, planned to provide broadband internet, intensifies the discussion even more [21]. Due to this problem scientists have developed models and concepts that are able to quantify the impact of objects that are inserted into the space environment. These include models such as the Criticality of Spacecraft Index (CSI), Environmental Consequences of Orbital Breakups (ECOB)/Debris Index and the Space Sustainability Rating (SSR). The most promising concept to be used in the future is the Debris Index, as it was selected as mission index module in the SSR framework commissioned by the World Economic Forum in 2018 [22]. The Debris Index is defined as the product of the **consequence** of fragmentations on operational satellites and the **likelihood** of these fragmentations to happen [23]. With ARES it is not possible to compute the parameters of the debris index in such a detail as it is done in [23]. However, in order to develop a metric similar to the debris index, the impact of a collision between a spacecraft and debris object on the space environment will be assessed through [24]

$$Risk = Likelihood \cdot Consequence\,. \qquad (7)$$

The **likelihood** of a collision is a straightforward concept, which describes the collision probability between an object of interest and the space debris population. ARES provides several different collision probability metrics as stated in Table 2.8. Figure 5.1 shows the likelihood of a collision depending on the size of the debris objects.

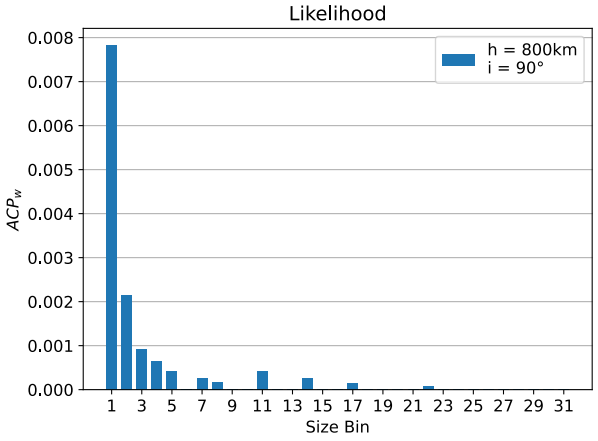

Figure 5.1 Annual collision probability caused by different size bins.

The likelihood is given in terms of the annual collision probability due to the whole population ACP_w between the minimum and maximum population sizes defined by the user. Of course, it is also possible to use ACP_d or ACP_m or any other fractional risk parameter (see Table 2.8) as likelihood metric depending on the analysis to be performed. It has to be mentioned that in the following Figures ACP_w has been used as likelihood metric, whereas throughout the derivation of the uncertainty requirements this will change to be the residual risk instead of the ACP_w. The size bin division is given in Table 5.1.

Table 5.1 Size bin division

Size Bin	d_{min} [m]	d_{repr} [m]	d_{max} [m]	Size Bin	d_{min} [m]	d_{repr} [m]	d_{max} [m]
1	0.01	0.015	0.02	17	0.17	0.175	0.18
2	0.02	0.025	0.03	18	0.18	0.185	0.19
3	0.03	0.035	0.04	19	0.19	0.195	0.20
4	0.04	0.045	0.05	20	0.20	0.205	0.21
5	0.05	0.055	0.06	21	0.21	0.215	0.22
6	0.06	0.065	0.07	22	0.22	0.225	0.23
7	0.07	0.075	0.08	23	0.23	0.235	0.24
8	0.08	0.085	0.09	24	0.24	0.245	0.25
9	0.09	0.095	0.1	25	0.25	0.255	0.26
10	0.1	0.105	0.11	26	0.26	0.265	0.27
11	0.11	0.115	0.12	27	0.27	0.275	0.28
12	0.12	0.125	0.13	28	0.28	0.285	0.29
13	0.13	0.135	0.14	29	0.29	0.295	0.3
14	0.14	0.145	0.15	30	0.3	0.305	0.31
15	0.15	0.155	0.16	31	0.31	0.315	0.32
16	0.16	0.165	0.17				

Collision **consequence**, however, is not clearly defined. It comprises several different definitions such as:

1. A collision between one or more massive objects which renders the operator's mission orbit unusable due to the large number of fragments posing high secondary collision likelihood with the operator's remaining orbit constellation [25].
2. A collision between one or more massive objects which renders the operator's mission orbit operationally untenable (i.e., too operationally challenging to manage, due to the

high analytical and Space Situational Awareness costs of identifying collision risks and repeatedly manoeuvring to avoid them) [25].

3. A collision with a mission-critical satellite which renders it ineffective or dead, causing the mission to be degraded or fail [25].

Within the scope of this work the first definition will be used to describe the consequence of a collision, since this definition is consistent with the collision consequence provided by [24]. The collision consequence is realized by computing the number of fragments that are generated as a result of a collision between spacecraft and debris object. The number of debris pieces greater than a specified size that a collision generates is defined as

$$N(L_c) = 0.1(P)^{0.75} L_c^{-1.71}\,, \tag{8}$$

where L_c is the characteristic length (size) above which one wishes to determine the number of debris pieces [24]. For this work the L_c will be set to 0.1 m, since it is assumed, that the minimum size for catalogued debris objects is limited to approximately 10 cm for LEO objects [26]. If the collision is catastrophic, the momentum factor P is the sum of the mass of the lighter satellite or debris object m and the mass of the larger satellite M [24]. If the collision is non-catastrophic, P is the product of the mass of the lighter satellite m and the conjunction's relative velocity V_{rel} [24]. The distinction between catastrophic and non-catastrophic collisions is assessed through the relative kinetic energy [24]

$$\frac{mV_{rel}^2}{2M} > 40000\frac{J}{kg}\,. \tag{9}$$

When the relative kinetic energy exceeds 40,000 Joules per kilogram, the collision is expected to be catastrophic and produce much larger amounts of debris [24].

In LEO, the average relative impact velocity between two space objects is 10 km/s [27, 28]. This value will be used for V_{rel} in equation (9).

The next step involves the calculation of the mass of the objects that could potentially collide with the spacecraft of interest. Therefore, a mass has to be assigned to each $d_{repr,i}$ from the size bin division from Table 5.1. Since ARES calculates internally the volume of space debris objects based on a sphere with $d_{repr,i}$ as diameter, it is only natural to calculate the mass with this volume

$$m = V_{sphere,i} \cdot \rho_i = \frac{4}{3} \cdot \pi \cdot \left(\frac{d_{repr,i}}{2}\right)^3 \cdot \rho_i\,. \tag{10}$$

The average mass density ρ_i for debris larger then 0.62 cm is

$$\rho_i = 2.8 \cdot {d_{repr,i}}^{-0.74}\,, \tag{11}$$

where ρ_i is given in g/cm^3 and $d_{repr,i}$ in cm [29]. Equation (11) assumes, that $d_{repr,i}$ is the diameter of a sphere. The resulting mass distribution is shown in Figure 5.2 depicted as green line. A problem lies in the assumption of a sphere. It must be questioned to what extent equation (11) can be applied for large $d_{repr,i}$ values. When looking into Figure 5.2, the green line seems to overestimate the mass for large $d_{repr,i}$. For example, it must be questioned whether it makes sense for an object with a representative diameter $d_{repr,i}$ of 80 m to have a mass of 1000 t. Especially because they are most likely not spherical objects with a diameter of 80 m, but rather elongated objects with a maximum length of 80 m in one dimension.

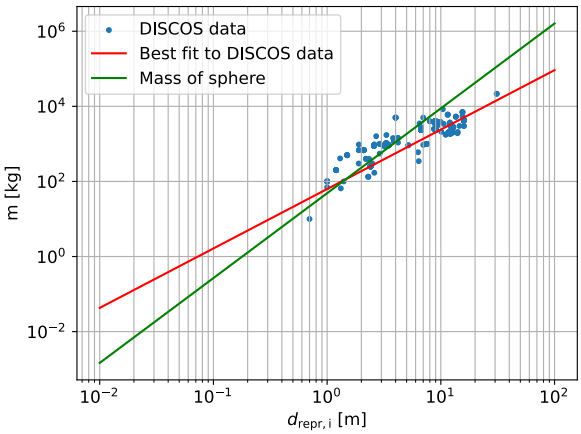

Figure 5.2 Mass distribution depending on $d_{repr,i}$

In order to model the mass of objects with a large $d_{repr,i}$ it is useful to consider space debris objects that are large and heavy. These objects include rocket bodies. Figure 5.2 shows the mass vs. $d_{repr,i}$ information of 393 rocket bodies, depicted as blue dots, which have been extracted from ESA's Database and Information System Characterizing Objects in Space (DISCOS). These data points have been gathered from (DISCOS) by filtering rocket body objects that have a re-entry epoch after 01.11.2016. This was done with the intention to be consistent with the reference epoch that ARES provides, which is also the 01.11.2016. By applying an exponential regression function of the form of

$$m_{regression} = a \cdot {d_{repr,i}}^{b}\,, \tag{12}$$

it is possible to derive a mass model for large objects depicted as red line in Figure 5.2, which delivers an R^2 value of 0.68. The regression function is defined through the parameters a = 62.76 and b = 1.58. Therefore, a combined mass distribution (see Figure 5.3) will be implemented, which is defined as

$$m_{combined} = \min\left(m, m_{regression}\right). \tag{13}$$

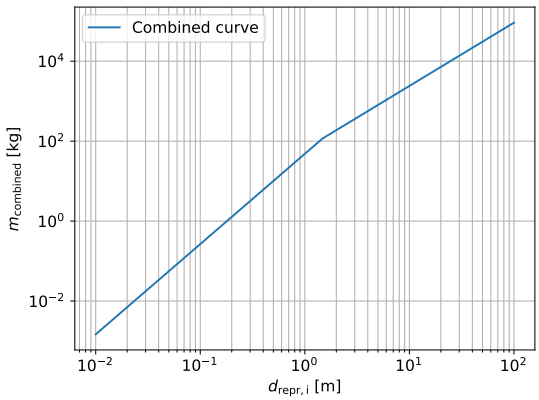

Figure 5.3 Combined mass distribution

Finally, it is possible to calculate the **consequence** in terms of the number of fragments that are generated as a result of a collision between spacecraft and debris object, which is shown in Figure 5.4.

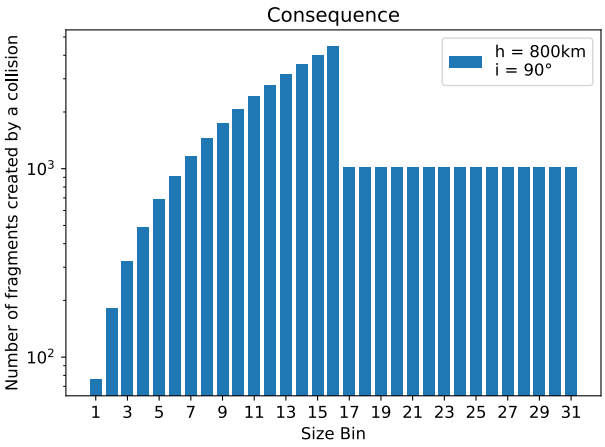

Figure 5.4 Number of fragments generated by a collision with an object characterized by the size bin

The next step consists of computing the risk in form of a risk matrix based on the product of likelihood and consequence. Before that, however, likelihood and consequence must be converted into a scoring scheme, which assigns their values to a score. The scoring scheme for the likelihood classification is based on [30] as it is shown in Table 5.2.

Table 5.2 Likelihood Scoring Scheme [30]

Score	Likelihood (Annual Collision Probability)
1	<0.0001
2	0.0001 – 0.001
3	0.001 – 0.01
4	0.01 – 0.1
5	>0.1

The consequence is not as straightforward to determine as the likelihood, because it has to be defined on a case-by-case basis as [30] suggests. The scoring scheme for the consequence classification is based on historic collision events and adjusted to the requirements of this work. The historic collision events have been extracted from [31] and [32] and are listed in Table 5.3. Note, that only those events are listed where it is known how many fragments have been catalogued.

Table 5.3 Historic collision events [31, 32]

Object	Year	Number of catalogued objects
Fengyun-1C	2007	3431
Cosmos-2251	2009	1667
Iridium-33	2009	627
Solwind	1985	284
DMSP 5B F5 R/B	1974	10
Cosmos-1934	1988	2
Cerise	1995	1
Nadezdha 2 R/B	1990	1
Sentinel-1A	2014	0

Based on the historic collision events it was decided to use a logarithmic division of the consequence score classification, as listed in Table 5.4. Here, a classification was pursued as presented in [30] consisting of the five severity classes: catastrophic (5), critical (4), major (3), significant (2) and negligible (1). It is assumed that an anti-satellite test like the one with Fengyun-1C and a collision like the one between Iridium-33 and Cosmos-2251 have a catastrophic impact on the space environment. For this reason, collisions creating more than 1000 objects that can be catalogued were classified as the most critical level with a scoring value of 5. This means, that Iridium-33 is classified in scoring class 2 due to the logarithmic classification. Collision events that create no detectable objects were classified as not fundamentally threatening to space operations with a scoring value of 1.

Table 5.4 Consequence Scoring Scheme

Score	Consequence
1	<1
2	1 – 10
3	10 – 100
4	100 – 1000
5	>1000

After classifying every data point from Figure 5.1 and Figure 5.4 to a likelihood and consequence score, it is possible to multiply both the likelihood score from Figure 5.5 and the consequence score from Figure 5.6, which creates a risk value.

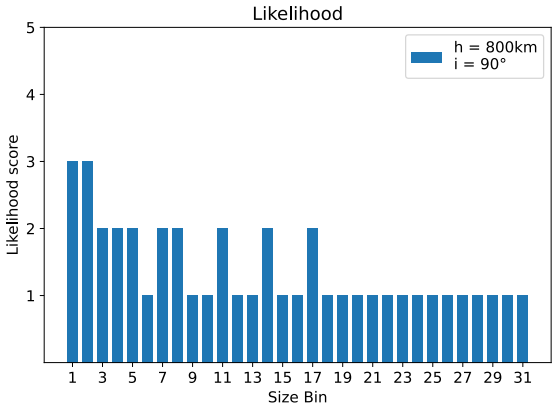

Figure 5.5 Likelihood score

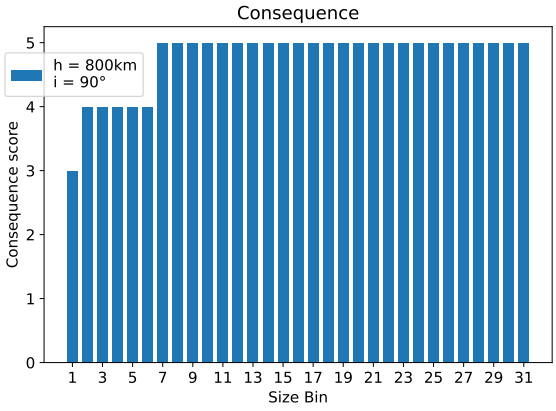

Figure 5.6 Consequence score

This multiplication of both the likelihood and the consequence score results in the risk score, depicted in Figure 5.7.

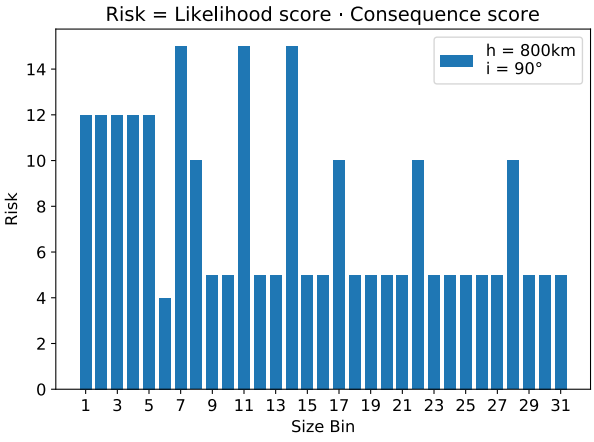

Figure 5.7 Risk = Likelihood score · Consequence score

Depending on the risk value it is possible to assess whether the impact of a collision on the environment is very low, low, medium, high or very high based on the classification provided in Table 5.5.

Table 5.5 Risk Matrix based on [30]

Risk = Likelihood · Consequence					
Consequence \ Likelihood	1	2	3	4	5
5	5 Low	10 Medium	15 High	20 Very High	25 Very High
4	4 Low	8 Low	12 Medium	16 High	20 Very High
3	3 Very Low	6 Low	9 Low	12 Medium	15 High
2	2 Very Low	4 Very Low	6 Low	8 Low	10 Medium
1	1 Very Low	2 Very Low	3 Very Low	4 Very Low	5 Low

Figure 5.7 shows the risk only for an orbital altitude of 800 km and an inclination of 90°. However, a better overview is obtained when looking at the risk classification of several orbital altitudes. This is depicted in Figure 5.8 as heat map.

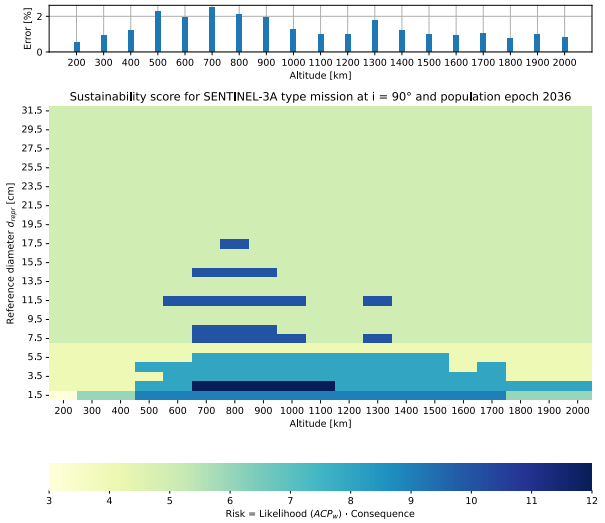

Figure 5.8 Risk heat map

When dividing the MASTER population into many small bins (Table 5.1), an error occurs in the calculation of the annual collision probability. It happens that the sum of the annual collision probability over the individual bins is not equal to the total annual collision probability, as described by

$$ACP_w(h) \neq \sum_{i=1}^{n} ACP_{w,i}(h)\,. \tag{14}$$

The error which quantifies the deviation between the total annual collision probability and the binned annual collision probability is shown in Figure 5.8 for every altitude individually above the sustainability score. Since the highest error is about 2%, it is assumed to be negligible.

Until now, the likelihood of the sustainability score was always defined as the annual collision probability related to the entire population from 0.01 m to 100 m (ACP_w). Another way to define the likelihood is to use the residual risk, which results from the choice of the ACPL. The ACPL defines the amount of residual and reduced risk, which adds up to ACP_d according to [14]. ACP_d is the annual collision probability defined by the flux that can be detected by the SSN. The usage of the residual risk as likelihood metric in the sustainability score, describes the impact on the environment by the risk of a collision induced by the objects that can be detected but are ignored because of the ACPL. Figure 5.9 shows the sustainability score with the residual risk as likelihood metric again for a Sentinel-3A type mission at an inclination of 90° and the epoch at 2036.

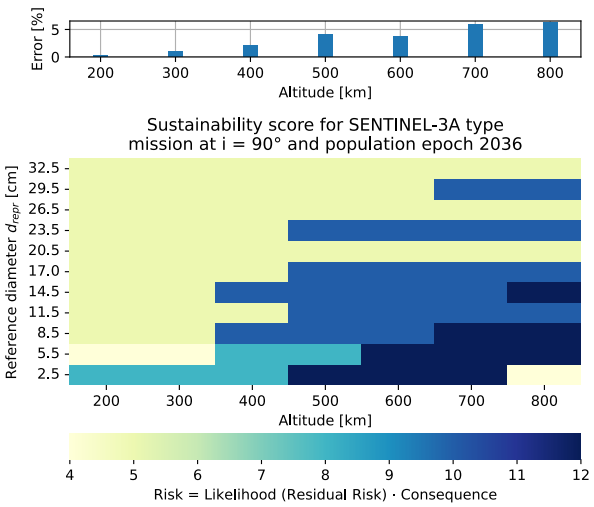

Figure 5.9 Sustainability score based on the residual risk as likelihood metric for an uncertainty distribution of AT = 1 km, CT = 0.4 km and RA = 0.2 km in every uncertainty class

With this diagram it is possible to vary the uncertainty of the SSN and to observe the change in risk on the space environment. It can therefore be analysed to what extent the uncertainty must be reduced in order to decrease the score/risk. For this, however, a constant ACPL must be chosen, as otherwise the residual risk will not change with varying uncertainty. The ACPL is therefore set to 0.0001 as in the previous sections.

Since the high uncertainty of small objects induces the greatest effect on the manoeuvre rate, the following analyses are limited to a reference diameter range between 1 cm and 34 cm. The population size classification is listed in Table 5.6 and has been optimized so that the binning error remains in the order of 5%.

Table 5.6 User defined size bin division

Size Bin	d_{min} [m]	d_{repr} [m]	d_{max} [m]	Size Bin	d_{min} [m]	d_{repr} [m]	d_{max} [m]
1	0.01	0.025	0.04	7	0.19	0.205	0.22
2	0.04	0.055	0.07	8	0.22	0.235	0.25
3	0.07	0.085	0.1	9	0.25	0.265	0.28
4	0.1	0.115	0.13	10	0.28	0.295	0.31
5	0.13	0.145	0.16	11	0.31	0.325	0.34
6	0.16	0.175	0.19				

The uncertainty table used for Figure 5.9 uses an uncertainty distribution of AT = 1.0 km, CT = 0.4 km and RA = 0.2 km in every uncertainty class from Table 2.4. The ratio between AT, CT and RA was defined throughout this work exactly as it is stored in the default setting of ARES. That is, the two minor axes make up 0.4 (CT) and 0.2 (RA) of the major axes of the covariance ellipsoid.

Note that the likelihood classes (Table 5.2) had to be adjusted to the residual risk, which is used throughout the current plots. Since the residual risk is only a part of the annual collision probability ACP_d, the lower limit of the likelihood classification had to be extended, which is shown in Table 5.7.

Table 5.7 Likelihood scoring scheme (residual risk)

Score	Likelihood (Residual risk)
1	<0.00001
2	0.00001 - 0.0002154
3	0.0002154 - 0.00464
4	0.00464 - 0.1
5	>0.1

6 DERIVATION OF UNCERTAINTY REQUIREMENTS

The first step consists of analysing to what extent the uncertainty must be reduced in order to get into the risk class ‘low’, which is the case for risk score values between 5 and 9 (see Table 5.5). For this purpose, the uncertainty is kept constant across the inclination and eccentricity classes, while the uncertainty is varied along the perigee altitude classes (see Table 2.4). Even if it does not correspond to reality that the uncertainty is constant across the inclination and the eccentricity classes, the sustainability score in its current form only provides information about the altitude and it simplifies the parameter variation.

The resulting sustainability score is depicted in Figure 6.1 and it shows that each region has a risk score smaller than 9. Figure 6.2 shows a clear representation of the uncertainty variation across the perigee altitude classes.

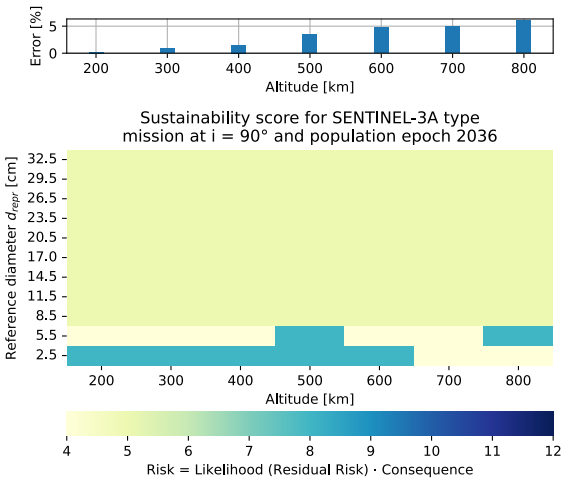

Figure 6.1 Sustainability score for the adjusted uncertainty table reaching a risk score of 8

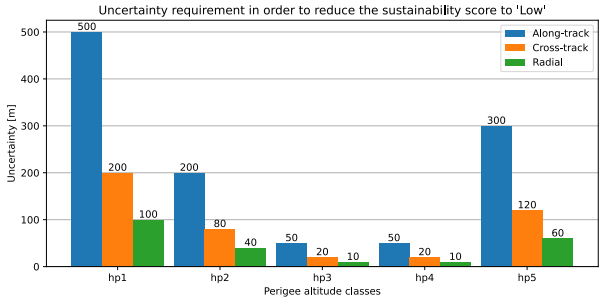

Figure 6.2 Uncertainty values depending on perigee altitude classes

The next step is to analyse to what extent the uncertainty has to be reduced until the risk score converges and remains constant regardless of further uncertainty reduction. The resulting sustainability score of this analysis is depicted in Figure 6.3 and it shows that each region has a risk score smaller than 5.

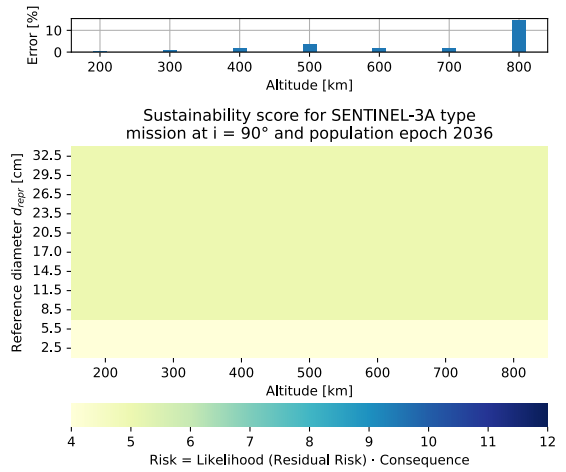

Figure 6.3 Sustainability score for the adjusted uncertainty table reaching a converging risk score

Figure 6.4 shows a clear representation of the uncertainty variation across the perigee altitude classes. It is observable, that the uncertainty in the perigee altitude class h_{p3} (550 km < h_{p3} ≤ 800 km) is the most stringent requirement with 12.25 m in along-track direction.

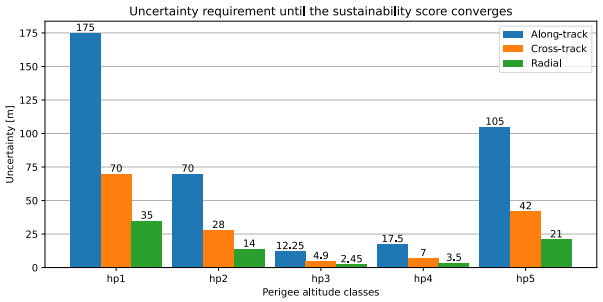

Figure 6.4 Uncertainty values depending on perigee altitude classes

Now that the requirements are known, they will be compared with current uncertainty values of publicly available CDMs. The CDMs originate from ESA's Advanced Concepts Competition Website called Kelvins and contain the along-track, cross-track and radial uncertainty values of a close encounter between two objects. The dataset was filtered by chaser objects representing space debris objects and only conjunctions with a time between event prediction and event occurrence of greater than 0.97 and less than 1.03 were considered to approximate a time of closest approach (TCA) of 1 as it was applied throughout the uncertainty requirement analysis. The perigee altitudes were then classified into the perigee altitude classes h_{px} as per Table 2.3. However, the dataset does not contain values for h_{p5} and h_{p6}. It has to be mentioned that, since the data contains some outliers, the uncertainty is not given as a mean value but as a median.

Table 6.1 shows a comparison between the publicly available uncertainty data and the required uncertainties for achieving a low and converging sustainability score depending on the altitude classes h_{p1} to h_{p5}. Since the highest uncertainty values exist in along-track direction, only these are listed and compared in Table 6.1.

Because of the atmospheric drag, orbit propagation is highly inaccurate at lower orbit altitudes ($h_{p1} \leq 350$ km). This leads to demanding requirements in this orbital region. While the current uncertainty values predict an uncertainty of 5521 m for a TCA of 1 day, the uncertainty has to decrease by a factor of 32 to 175 m for the sustainability score to converge (improvement of 96.8%). The situation is similar in the perigee altitude class h_{p3} (550 km < $h_{p3} \leq$ 800 km), where the uncertainty must be improved from 603 m to 12.25 m (improvement of 98%) in order to achieve a converging sustainability score.

Table 6.1 Uncertainty comparison in along-track direction at TCA = 1 day

Perigee altitude class	h_{p1}	h_{p2}	h_{p3}	h_{p4}	h_{p5}
Publicly available uncertainty (median) **[m]**	5521	1035	603	358	-
Uncertainty requirement: Sustainability score = Low**[m]**	500	200	50	50	300
Uncertainty requirement: Converging sustainability score **[m]**	175	70	12.25	17.5	105

7 SUMMARY AND OUTLOOK

One of the objectives of this work was to determine the number of manoeuvres that occur as a result of the SSN being upgraded with the new Space Fence. For this purpose, ESA's ARES software was used to compute the manoeuvre rate. The performance of the Space Fence was estimated from a comprehensive literature review. The literature search revealed that the new SSN is modelled by using a radar wavelength of 0.15 m, a reference diameter of 0.26 m and an unchanged uncertainty compared to the current SSN.

The analysis carried out for the epoch 2022 and an ACPL of 0.0001 results in the highest manoeuvre rates, counting between 1 and 2.4 manoeuvres per year at an altitude of 800 km. If the epoch is adjusted to 2036 (i.e. MASTER's future population forecast in 14 years), the manoeuvre rate remains in the same order of magnitude. Improving the wavelength and the reference diameter always leads to an increase in manoeuvre rate because a larger flux is detected. The uncertainty, however, is the only parameter of the SSN model that reduces the manoeuvre rate, which makes it an important parameter to improve.

In order to derive requirements regarding the uncertainty of future SSN, a sustainability score was developed that assesses the impact of a collision on the space environment by combining the consequence of a collision with the probability that this collision will occur. The consequence is defined as the number of fragments created during the collision and the probability is defined as an annual collision probability metric or fractions thereof. The likelihood and consequence values are then classified into a likelihood and consequence score, with the product of both, forming the sustainability score or simply called "risk".

It is then possible to derive uncertainty requirements from the sustainability score, using the residual risk as likelihood. The uncertainty is reduced until an acceptable risk level is reached or the score converges. The most stringent uncertainty requirements are at the perigee altitude class h_{p3} (550 km < h_{p3} ≤ 800 km). A low-level risk score is reached for an uncertainty in along-track direction of 50 m, whereas convergence is reached for 12.25 m.

The extent to which the uncertainty requirements are achievable cannot be assessed yet. The requirements demand for an improvement in uncertainty of over 90% compared to publicly available conjunction data messages (CDM). The Commercial Space Operations Center (COMSpOC) proposes sensor fusion techniques that are capable of reducing the position uncertainty by merging government, commercial and satellite operator data of multiple different sensor types (radar, ground-based optical, space-based optical and passive RF) [33]. Additionally, through the use of advanced data processing techniques, it is possible to reduce the uncertainty in LEO by 10% to 50% [33]. Whether an improvement of 90% is achievable needs to be investigated in the future.

8 ACKNOWLEDGMENTS

The research leading to these results was supported by the European Space Agency (ESA) within the CASCADE GSTP study under ESA Contract No. 4000139430/22/D/SR.

9 REFERENCES

1. Verspieren, Q.: A Reluctant Safety Services Provider: The Role of the Military in Space Traffic Management. Dissertation, The University of Tokyo (2020)
2. GAO: Development and Oversight Challenges in Delivering Improved Space Situational Awareness Capabilities. United States Government Accountability Office. https://www.gao.gov/assets/gao-11-545.pdf (2011). Accessed 11 April 2022
3. Weeden, B.: Space Situational Awareness Fact Sheet. Space Situational Awareness Fact Sheet, 2017-05. https://swfound.org/media/205874/swf_ssa_fact_sheet.pdf. Accessed 3 April 2022
4. Fonder, G., Hughes, M., Dickson, M., Schoenfeld, M., Gardner, J. (eds.): Space Fence Radar Overview. International Applied Computational Electromagnetics Society Symposium, Miami, FL, USA, 14-19 April 2019. IEEE (2019)
5. Hejduk, M.D.: Conjunction Assessment Space Fence Update, 2019. https://ntrs.nasa.gov/api/citations/20190033388/downloads/20190033388.pdf. Accessed 4 June 2022
6. Shimkus, K.: USSF announces initial operational capability and operational acceptance of Space Fence. https://www.spaceforce.mil/News/Article/2129325/ussf-announces-initial-operational-capability-and-operational-acceptance-of-spa (2020). Accessed 4 April 2022
7. Zimmer, P. (ed.): GPU-accelerated Faint Streak Detection for un-cued Surveillance of LEO. Advanced Maui optical and space surveillance technologies, Mau, Hawaii, 10 - 13 September, Kihei, Hawaii (2014)
8. NASA: NASA's efforts to mitigate the risks posed by orbital debris.

National Aeronautics and Space Administration, Washington, D.C. https://oig.nasa.gov/docs/IG-21-011.pdf (2021)

9. Gonzalo, J.L., Colombo, C., Di Lizia, P.: Analytical Framework for Space Debris Collision Avoidance Maneuver Design. Journal of Guidance, Control, and Dynamics (2021). https://doi.org/10.2514/1.G005398
10. Fonder, G.P., Hack, P.J., Hughes, M.R. (eds.): AN/FSY-3 Space Fence System – Sensor Site One / Operations Center Integration Status and Sensor Site Two Planned Capability. Advanced Maui Optical and Space Surveillance Technologies Conference (AMOS), Maui, Hawaii, 19 - 22 September 2017 (2017)
11. Pelton, J.N.: Tracking of Orbital Debris and Avoidance of Satellite Collisions. In: Pelton, J.N., Madry, S., Camacho-Lara, S. (eds.) Handbook of Satellite Applications, pp. 1–13. Springer New York, New York, NY (2016)
12. Koltiska, M.G., Du, H., Prochada, D., Kelly, K. (eds.): AN/FSY-3 Space Fence System Support of Conjunction Assessment. Advanced Maui Optical and Space Surveillance Technologies Conference (AMOS), Maui, Hawaii, 20 - 23 September 2016 (2016)
13. NASA Science: Radio Frequencies. Section 1: Environment, Chapter 6: Electromagnetics. Electromagnetics. https://solarsystem.nasa.gov/basics/chapter6-3/ (2022). Accessed 5 June 2022
14. ARES: Assessment of Risk Event Statistics (ARES) Technical Note. European Space Operations Centre (ESOC), Darmstadt (2019)
15. ESA: Collision avoidance requirements verification and guidelines based on DRAMA/ARES. European Space Agency (ESA) (2020)
16. SpaceTrack: Sentinel-3A Orbit Mean-Elements Message (OMM). https://www.space-track.org/basicspacedata/query/class/gp/NORAD_CAT_ID/41335/format/xml/emptyresult/show (2022). Accessed 8 April 2022
17. ESA/ESOC Space Debris Office (OPS-SD): Debris Risk Assessment and Mitigation Analysis (DRAMA) Software User Manual. European Space Agency (ESA), Darmstadt, Germany (2022)
18. Merz, K., Virgili, B., Braun, V. (eds.): Risk reduction and collision risk thresholds for missions operated at ESA. Australian Aerospace Congress, Melbourne, 24-28 February 2019. European Space Agency (ESA), Darmstadt (2019)
19. Merz, K., Virgili, B., Braun, V., Flohrer, T., Funke, Q., Krag, H., Lemmens, S., Siminski, J. (eds.): Current Collision Avoidance service by ESA's Space Debris Office. 7th European Conference on Space Debris, Darmstadt, 18–21 April. ESA Space Debris Office, Darmstadt (2017)
20. IRAS/TUBS: Final Report. Enhancement of S/C Fragmentation and Environment Evolution Models. European Space Agency (ESA). https://sdup.esoc.esa.int/master/downloads/documentation/8.0.3/MASTER-8-Final-Report.pdf (2020). Accessed 10 April 2022
21. Flohrer, T., Sanchez-Ortiz, N., Dominguez-Gonzalez, R. (eds.): Effect of Mega Constellations on Collision Risk in Space. 8th European Conference on Space Debris, Darmstadt, Germany, 20–23 April 2021. ESA Space Debris Office, Darmstadt (2021)
22. Letizia, F., Lemmens, S., Wood, D., Rathnasabapathy, M., Lifson, M., Steindl, R., Acuff, K., Jah, M., Potter, S., Khlystov, N. (eds.): Framework For The Space Sustainability Rating. 8th European Conference on Space Debris, Darmstadt, Germany, 20–23 April 2021. ESA Space Debris Office, Darmstadt (2021)
23. Letizia, F., Colombo, C., Lewis, H., Krag, H.: Development of a Debris Index. Stardust Final Conference - Advances in Asteroids and Space Debris Engineering and Science (2018). https://doi.org/10.1007/978-3-319-69956-1_12
24. NASA: NASA Spacecraft Conjunction Assessment and Collision Avoidance Best Practice Handbook. National Aeronautics and Space Administration, Washington DC. https://nodis3.gsfc.nasa.gov/OCE_docs/OCE_50.pdf (2020)
25. Oltrogge, D.L., Alfano, S., Law, C., Cacioni, A., Kelso, T.S.: A comprehensive assessment of collision likelihood in Geosynchronous Earth Orbit. Acta Astronautica (2018). https://doi.org/10.1016/j.actaastro.2018.03.017
26. Hasenohr, T.: Initial Detection and Tracking of Objects in Low Earth Orbit. Master, University of Stuttgart. https://elib.dlr.de/110661/1/Initial%20Detection%20and%20Tracking%20of%20Objects%20in%20Low%20Earth%20Orbit.pdf (2016). Accessed 1 April 2022
27. Firooz A. Allahdadi, Isabelle Rongier, Paul D. Wilde (eds.): Safety Design for Space Operations. Butterworth-Heinemann, Oxford (2013)
28. Letizia, F., Colombo, C., Lewis, H.G., Krag, H.: Assessment of breakup severity on operational satellites. Advances in Space Research (2016). https://doi.org/10.1016/j.asr.2016.05.036
29. Anderson, J.B., Smith, R.E.: Natural Orbital Environment Guidelines for Use in Aerospace Vehicle Development. NASA, Alabama. https://ntrs.nasa.gov/api/citations/19940031668/downloads/19940031668.pdf (1994). Accessed 24 June 2022
30. ECSS: Space project management. Risk management. European Cooperation for Space Standardization, Noordwijk, The Netherlands. http://everyspec.com/ESA/download.php?spec=ECSS-M-ST-80C.047919.pdf (2008). Accessed 26 June 2022
31. ESA: Fragmentation event database statistics. https://fragmentation.esoc.esa.int/home/statistics (2022). Accessed 22 August 2022
32. Anz-Meador, P.D., Opiela, J.N., Shoots, D., Liou, J.-C.: History of on-orbit satellite fragmentations. NASA, Houston, Texas. https://orbitaldebris.jsc.nasa.gov/library/20180008451.pdf (2018). Accessed 22 August 2022
33. Oltrogge, D.L., Wauthier, P., Vallado, D.A., Alfano, S., Kelso, T.S. (eds.): Results of Comprehensive STCM Data Fusion Experiment. 8th European Conference on Space Debris, Darmstadt, Germany, 20-23 April 2021. ESA Space Debris Office, Darmstadt (2021)